LAWRENCE
LIVERMORE
NATIONAL
LABORATORY

LLNL-JRNL-831224

Simulating the filamentation of smoothed laser beams with three-dimensional nonlinear dynamics

L. J. Babati, W. A. Farmer, R. L. Berger, M. A. Belyaev, T. Chapman, D. E. Hinkel, E. Kur, E. A. Williams

January 27, 2022

AIP Advances

Disclaimer

Simulating the filamentation of smoothed laser beams with three-dimensional nonlinear dynamics

L. J. Babati,[1,2] W. A. Farmer,[2] R. L. Berger,[2] M. A. Belyaev,[2] T. Chapman,[2] D. E. Hinkel,[2] E. Kur,[2] and E. A. Williams[2]

[1)] *UC Santa Barbara, Department of Physics, Santa Barbara, CA 93106, USA*

[2)] *Lawrence Livermore National Laboratory, 7000 East Ave., Livermore, CA 94550, USA*[a)]

(Dated: 30 August 2022)

In a plasma, the ponderomotive force of an inhomogeneous electromagnetic field expels plasma from regions of high intensity. When a laser propagates through a plasma, this force creates density wells that subsequently modify the index of refraction. The beam refracts and focuses into these wells and may filament. In extreme cases, the laser beam will spray due to increasing angular divergence of the beam. The threshold for ponderomotive self-focusing is well established for isolated laser hotspots or speckles. Here, we define a practical threshold for characterizing the filamentation of thousands of speckles that are found in the focal plane of high-power laser beams spatially smoothed with random phase plates as used at high energy and power laser facilities studying inertial confinement fusion (ICF). This threshold is tested against three-dimensional simulations of speckled laser light propagating through plasma. Four metrics are applied to assess filamentation: the fraction of power above five times the average intensity, an effective f-number, the mean-squared perpendicular wave number, and the fraction of rarefied density with deviation from the initial density exceeding $|\delta n/n| = 0.1$. The speckled beams studied are generated by random phase plates, both with and without additional polarization smoothing, in a parameter regime of relevance to indirect drive experiments. While filamentation has been discussed extensively in the literature, we believe this to be the first published simulation study with three-dimensional nonlinear hydrodynamics that addresses the onset threshold of ponderomotive filamentation and establishes the lengths and time scales necessary to reach a statistical steady state.

I. INTRODUCTION

Lasers have been used extensively in scientific investigations of a wide variety of physical phenomena[1–6]. As laser light propagates through plasma, laser-plasma instabilities (LPI) can occur[7–10]. Of these instabilities, self-focusing and subsequent filamentation can amplify transverse variations in the laser intensity. The self-focusing may arise due phenomena including ponderomotive and thermal forces or relativistic effects in the plasma. Here, we study plasma and laser parameters such that the ponderomotive force drives the filamentation[11–14]. In experiments where filamentation occurs, laser decoupling to the target can compromise the experimental objectives[15].

In the absence of beam smoothing techniques, phase front aberrations at the lens will produce large-scale intensity variations across the spatial profile of a laser spot. In turn, these intensity variations drive modulations in the refractive index of the plasma that focus the laser light and can further exacerbate undesirable LPI. To mitigate this, smoothing techniques are used. Phase plates produce well-controlled and reproducible focal spot profiles with a specified shape and size[16–18] and are used in all high-power ICF laser facilities[19–21]. These phase plates create a speckle pattern of the beam with the typical speckle width and length being approximately $f\lambda_0$ and $8f^2\lambda_0$, respectively, where f is the f-number of the laser and is defined by the ratio of the phase plate size to the focal length[22]. Additionally, polarization smoothing (PS) can be used to scramble the phase correlation between two orthogonal polarizations, reducing the coherent intensity interacting with the plasma[23,24], and temporal smoothing may also be applied[25].

The typically applied practical threshold for the onset of ponderomotive filamentation[26] examined in this study is given by,

$$Q = \frac{I[\mathrm{W/cm^2}]\lambda_0^2[\mu\mathrm{m}^2]}{10^{13}[\mathrm{W}\mu\mathrm{m}^2/\mathrm{cm}^2]} \frac{3\ \mathrm{keV}}{(T_e + T_i/\bar{Z})[\mathrm{keV}]} \frac{n_e}{n_c} \left(\frac{f}{8}\right)^2, \tag{1}$$

where I is the average intensity of the beam, and Q is defined as the filamentation figure of merit; also T_e and T_i are respectively the electron and ion temperatures, $\bar{Z}$ is the mean ionization state, n_e is the electron number density, n_c is the critical density and λ_0 is the wavelength of the light. Here, the specific heat ratios of the electrons and ions (discussed later) have been set to unity. Ref. 26 reported the threshold for a beam smoothed by phase plates is $Q = 1$, and with PS, $Q = 1.6$ based on undocumented pF3D[10,13,27] simulations. Here, we present in detail simulations qualifying and supporting these thresholds and examine cases up to $Q{\sim}4$.

We arrive at the threshold in Eq. (1) by considering unmagnetized plasma with non-relativistic laser intensities relevant to ongoing inertial confinement fusion experiments which produce underdense plasma at keV temper-

[a)] farmer10@llnl.gov

atures. In the presence of an inhomogeneous, oscillating electric field, the electrons respond to the ponderomotive potential,

$$\phi_p = \frac{e^2 \left\langle E^2 \right\rangle}{2m\omega^2}, \tag{2}$$

where e and m are the respective unsigned charge and mass of an electron, ω is the angular frequency of the light, and $\left\langle E^2 \right\rangle$ denotes a temporal average of the electric field over time scales long relative to the period of oscillation. This ponderomotive potential expels electrons from regions of high-intensity, creating a spatially varying index of refraction that acts as a lens and subsequently focuses the laser into these density wells. So long as the self-focusing distance is shorter than the Rayleigh length, self-focusing occurs. Combining estimates of these two quantities results in a threshold for self-focusing[12–14,28,29],

$$\left(\frac{mv_o^2}{\gamma_e T_e + \gamma_i T_i/\bar{Z}}\right) \frac{n_e}{n_c} \left(\frac{L}{\lambda_0}\right)^2 > C, \tag{3}$$

where $v_o = eE/m\omega$ is the oscillatory velocity of an electron, L is the characteristic transverse length scale of the intensity distribution, here taken as $f\lambda_0$. C is a numerical constant of order unity; its value may be determined by simulations and is sensitive to additional properties of the laser discussed below.

Rewriting Eq. (3) in appropriate units, one obtains Eq. (1). The dependence on T_i from the ion pressure is often neglected, but in plasmas with $\bar{Z} \sim 1$ and comparable electron and ion temperatures, as is the case in the following, this additional term is important. For the parameters chosen in this study, $\gamma_e = 1$ is appropriate due to the isothermal behavior of the electrons (discussed later). In prior work[28], $\gamma_i = 1$ was also assumed. In the following, C (or equivalently, Q) is evaluated using $\gamma_i = 1$; C changes by ∼10% if $\gamma_i = 5/3$ (appropriate for a monotomic gas model with three degrees of freedom) is instead used.

Filamentation may be enhanced or even predominantly driven by thermal self-focusing. Estabrook *et al.*[30] showed with two-dimensional (2D) nonlinear fluid hydrodynamics, flux-limited Spitzer-Härm heat conduction, and light wave ray tracing that inverse bremsstrahlung heating of underdense plasma caused a plasma gradient perpendicular to the laser propagation direction that subsequently focuses the light. Filamentation of spatially and temporally smoothed beams in regimes where thermal effects are important has been studied[31,32] using paraxial light wave propagation and a linearized plasma density response and flux-limited Spitzer-Härm heat conduction. In general, when "classical" heat conduction is used, ponderomotive forces remain dominant on the small laser speckle scales which self focus in ∼10 ps rather than a few nanoseconds for whole beam self focusing. With a Vlasov Fokker-Planck (VFP) treatment of the electrons that captures nonlocal transport, thermal filamentation was recognized as potentially as important as ponderomotive at the speckle size[33]. Subsequent theoretical analysis with linearized VFP equations confirmed this result and developed formulae that modified hydrodynamic coefficients such as the thermal conductivity and viscosity[34–39]. Simulation work of smoothed laser beam propagation using a linearized solution to the VFP equation and a nonlinear plasma density response has also been carried out[40]. In this work, the chosen plasma parameters result in sufficient heat conduction such that ponderomotive filamentation is the dominant filamentation mechanism.

To date, fully kinetic simulations of filamentation have largely been restricted to 2D because of computational cost. In addition to VFP, particle-in-cell simulations have also been used to study the ponderomotive filamentation of a Gaussian beam in 2D[41,42]. While kinetic numerical methods may more naturally describe the rich physics of the plasma response, the applications of interest here where the filamentation of thousands of speckles of light produced by spatially smoothed beams is studied preclude such methods due to the limits of current computational feasibility. Recent research has also been carried out into the impact of multi-ion species kinetic effects on the filamentation of speckled laser light using a multi-fluid hydrodynamic model in a 2D geometry[43].

This paper presents a detailed 3D study of ponderomotive filamentation using pF3D simulations of a laser beam propagating through a plasma described by a nonlinear hydrodynamic model. Above the threshold for filamentation, density holes as low as 20% of the initial density are observed, illustrating the necessity of the nonlinear treatment. Four metrics are defined to assess filamentation: the fraction of power above intensity (FOPAI) used previously[29], an effective f-number[44], the mean-square of the transverse wave number of the beam, determined by Fourier analysis, and the fraction of rarefied density with deviation from the initial density exceeding $|\delta n/n| = 0.1$. The metrics are used to determine thresholds for filamentation. Prior simulation work has also studied the threshold of filamentation and subsequent evolution of the beam in Fourier (k) space[44,45], but was restricted to two spatial dimensions, which alters the threshold. In order to do a focused study on ponderomotive filamentation, backscatter processes such as stimulated Raman scattering (SRS) and SBS are neglected in the simulations. Inverse bremsstrahlung heating[46] is also neglected to eliminate thermal filamentation[30,33] and to keep the spatially averaged temperature constant.

The paper is organized as follows. Section II describes the simulations and justifies the neglect of thermal filamentation for the chosen plasma parameters. The metrics are defined in Sec. III with details of temporal and spatial convergence given in Appendix A. The results are given in Sec. IV with conclusions summarized in Sec. V.

II. SIMULATION SETUP

To study filamentation, the massively parallel laser plasma interaction code pF3D[27] is used with the laser propagation described by a near-paraxial light model[47]. Because of the well-separated timescales between the ion dynamics within speckles and the light crossing time, simulation results are unchanged whether the light propagation is assumed instantaneous or it propagates at the speed of light. The laser light is coupled to the background plasma which is described in the fluid approximation but using the full nonlinear hydrodynamic equations[48]. pF3D provides a variety of additional physics models and allows for versatility in describing the laser profile making it well-suited for examining ponderomotive filamentation.

For a single fluid (as used in this study), pF3D solves a set of fluid equations,

$$\frac{\partial \rho_i}{\partial t} + \nabla \cdot (\rho_i \mathbf{v}) = 0, \tag{4a}$$

$$\partial_t (\rho_i \mathbf{v}) + \nabla \cdot (\rho_i \mathbf{v} \otimes \mathbf{v}) + \nabla p = \mathbf{p}_f + \mathbf{d}, \tag{4b}$$

$$\partial_t \left(\frac{3}{2} p + \frac{1}{2} \rho_i u^2 \right) + \nabla \cdot \left[\left(\frac{5}{2} p + \frac{1}{2} \rho_i u^2 \right) \mathbf{v} \right] = \tag{4c}$$

$$\mathbf{v} \cdot [\mathbf{p}_f + \mathbf{d}] - \nabla \cdot \mathbf{q}_e + d_e + s_e,$$

$$\frac{3}{2} \left[\partial_t p_i + \nabla \cdot (p_i \mathbf{v}) \right] + p_i \nabla \cdot \mathbf{v} = d_e + \nu_{ei} \left[p - (1 + \bar{Z}) p_i \right], \tag{4d}$$

where the ion pressure equation is chosen to be the auxiliary energy relation. Since $p_i \ll p_e$, this has numerical advantages when decomposing p into its constituent partial pressures. These six differential equations for six unknowns (ρ_i, $\mathbf{v}$, p_i, and p) are supplemented by the algebraic relationships,

$$n_e = \bar{Z} \rho_i / \bar{A}, \qquad \text{(quasineutrality)} \tag{5a}$$

$$p_e = p - p_i, \qquad \text{(Dalton's Law)} \tag{5b}$$

$$T_e = p_e / ne, \qquad \text{(Boyle's Law)} \tag{5c}$$

the sums for effective local material properties, and suitable definitions for the sources $\mathbf{p}_f$, $\mathbf{d}$, d_e, and s_e where $\mathbf{p}_f$ is the ponderomotive force, $\mathbf{d}$ represents the Landau damping of the momentum, d_e is the rate of Landau damped kinetic energy deposited into ion thermal energy, s_e is the energy absorbed by inverse bremsstrahlung from the laser, and $\mathbf{q}_e$ is the electron heat flow. The behavior of the electron temperature depends of the ratio of the scale of the perturbation relative to the electron-ion mean free path. If the electron heat flow is large, temperature variations are rapidly smoothed resulting in an approximately isothermal plasma. On the other hand, if the heat flow is weak, the electron temperature tends to the adiabatic limit.

In the simulations reported here, the plasma is composed of fully ionized hydrogen with $n_e = 0.1 \times n_c$, $T_e = 3$ keV, and an ion temperature of $T_i = 1.5$ keV with no initial plasma flow. Under these conditions, the electron-ion mean free path for a thermal electron is 180 μm. A nonlocal coupling coefficient, A_k, can be employed as described in Ref. 38 to estimate the enhancement of the linear growth rate of filamentation due to thermal effects. For our plasma parameters and assuming the half-wave length of the growing perturbation cannot exceed the speckle width, we find a maximum possible increase of A_k due to thermal effects relative to the purely ponderomotive limit of 9%, consistent with our choice to suppress inverse bremsstrahlung heating and thermal filamentation. The ion-ion mean free path is 54 μm, an order of magnitude larger than the speckle width. For simplicity, the ion heat flow is neglected in Eq. (4d). We compared simulations with and without ion heat flow turned on and did not observe a significant impact of this process on filamentation for the parameters considered.

This study used a box size of $2048 \times \lambda_0 = 0.72$ mm in the transverse direction and $0.72 - 1.44$ mm in the axial direction, with $\lambda_0 = 351$ nm, corresponding to the third harmonic of a neodymium laser medium and the wavelength used at both the National Ignition Facility (NIF)[19], the Laser Mega Joule(LMJ)[21], and OMEGA[20]. This axial distance is four to eight speckle lengths for an $f = 8$ beam for reasons discussed in Sec. IV and allows for the observation of filamentation while minimizing the growth lengths of forward stimulated Brillouin scattering (SBS), which is beyond the scope of this study. The light propagates in the z direction, and x and y are the transverse directions. Because forward SBS grows from thermal fluctuations of the plasma, numerical noise, or transient waves caused by the localized expulsion of plasma from the laser ponderomotive force, significant amplification occurs over distances much longer than a speckle length. Further, the spatial growth rate is inversely proportional to the ion acoustic wave (IAW) damping rate which also suppresses FSBS in the simulations reported here.

Cell sizes of $\Delta x = \Delta y = 0.5\lambda_0$ and $\Delta z = 4\lambda_0$ are used in the main study. This choice is made based on a convergence study described in Appendix A. The electromagnetic boundary conditions are chosen to be periodic in the transverse directions and outflowing longitudinally. Boundary conditions for the fluid equations are also chosen to be periodic in the transverse direction. To prevent plasma flowing out of the domain, reflecting boundary conditions are imposed on the fluid equations in the longitudinal direction. Other choices were found to lead to temporal variations in metrics as the total amount of plasma decreased with time.

Using the plasma conditions chosen for these simulations, the threshold determined by Eq. (1) is 50% higher than would have been the case if T_i were neglected. The simulations are run for at least 100 ps so transient IAWs sufficiently damp and the plasma reaches a statistical steady state. The ponderomotive force is included in the fluid equations to allow for filamentation. Landau damp-

ing, included as the source term $\mathbf{d}$ in Eqs. (4)b and (4)c, is in practice applied in Fourier space and acts on all modes,

$$\frac{\partial \tilde{\mathbf{v}}_\perp}{\partial t} = -\eta \bar{c}_s \frac{\mathbf{k}_\perp}{k_\perp} \mathbf{k}_\perp \cdot \tilde{\mathbf{v}}_\perp, \tag{6}$$

where $\tilde{\mathbf{v}}_\perp$ is the Fourier amplitude of the transverse flow velocity, $\mathbf{k}_\perp = k_x \hat{\mathbf{x}} + k_y \hat{\mathbf{y}}$ is the transverse k-vector, $\bar{c}_s$ is the sound speed of an IAW averaged over the transverse plane, and η is a constant set in the simulation that is equal to the ratio of the damping rate to the oscillatory frequency. The kinetic energy lost due to Landau damping is conserved via an increase in ion thermal energy. A relatively high damping rate, $\eta = 0.2$, is applied in the cases shown here, appropriate for the damping of long wave length IAWs (i.e., $k\lambda_{De} \ll 1$, where k is the ion acoustic wave number and λ_{De} is the Debye length) in a hydrogen plasma where $T_e/T_i = 2$. In our simulations, electron heat conduction modifies the IAW response by effectively making the electrons isothermal. It is also included in a linearized form by Fourier transform. Any modification to the heat flux due to nonlocality[49] is neglected.

An $f = 8$ circular random phase plate (RPP) with 12801 elements is used to create a speckle pattern representative of experimental facilities such as the NIF. For simplicity, we consider here RPPs, where the phase imparted to the electric field at the lens is a random pattern of either 0 or π. This RPP beam fills the entire physical box with no spatial envelope defining the spot, and the beam is described as a disk with radius $1/(2f)$ in k-space. In addition, polarization smoothing can also be imposed; this splits the beam into two orthogonal polarizations that do not interact with each other[23]. This is done in the simulation by creating two beams with orthogonal polarizations. The beams are then offset relative to each other by 45 wavelengths in the y-direction and the resulting intensity is the incoherent sum of the two beams. The power in each beam is reduced by two relative to a beam without polarization smoothing so that the total power and spatially averaged intensity of the superimposed beams are unchanged.

Before illustrating a realistic RPP beam, self-focusing in the presence of a single Gaussian spot is shown. The interpretation of filamentation for RPP beams usually invokes the behavior of individual speckles of varying intensity that are thought of as Gaussian spots of intensity with $r_{\rm spot} = f\lambda_0/2$ such that $|E_0(x,y)|^2 = \exp(-\zeta(x^2 + y^2)/r_{\rm spot}^2)$. With $\zeta = \log(2)$, the intensity is one-half the peak value at $r = \sqrt{x^2+y^2} = r_{\rm spot}$. The nonlinear stability of Gaussian spots was shown to depend on the power in the spot with the threshold power given by[28]

$$P_c = c\, n_c (T_e + T_i/Z) \frac{n_c}{n_e} \frac{\lambda_0^2}{\pi} \sqrt{1 - \frac{n_e}{n_c}} \tag{7}$$

$$= 7.6 \times 10^8 \mathrm{W} \tag{8}$$

where the value in Watts is determined with the parameters earlier in this section. For a peak intensity of 2×10^{15} W/cm^2, the power in the speckle is $P_{spec} = 1.78 \times 10^8$ W, about 25% of the threshold power.

pF3D simulations of a single $f = 8$ Gaussian speckle at 1.8×10^9 W, about twice the threshold power are shown in Fig. 1 after self-focusing has occurred. The peak intensity at the focus has increased and, just after, the beam breaks into a ring. In an RPP beam with average intensity of 2×10^{15} W/cm^2, there are few speckles with such an intensity for these plasma conditions. The extreme symmetry in this case will be broken in a realistic simulation where the beam at focus will have aberations that will break up the ring formation into a ring of beads. The threshold power, P_c, for a single Gaussian in Eq. (7) has the same scaling as the threshold Q in Eq. (1), and thus speckles with twice P_c are expected to break into smaller speckles with less power but not necessarily less intensity. Further, Fig. 1(c) shows the density depression that occurs in the self-focusing region illustrating the need for a nonlinear hydrodynamic treatment.

In Fig. 2, an example of the propagation of an RPP beam is shown. The vertical axis is the propagation direction, and the horizontal axis is the orthogonal x-direction for a slice at $y = 0$. Only one-fourth of the width is shown so that the size and intensity of the speckles are visible. For the first speckle length, the intensity of the more unstable speckles increases without much visible decrease in the length. The second speckle length shows a dramatic decrease in the speckle size and increase in the number, consistent with the behavior of the individual Gaussian speckles previously considered. The behavior in this RPP case is more dynamic because the filamented beams are creating smaller scale plasma holes as the light waves interfere constructively.

The speckle pattern of an RPP beam in the plane perpendicular to the propagation axis is shown in Fig. 3 with the top and middle panels showing the speckle pattern at the entrance plane and at the exit plane, respectively, and the bottom panel, the electron density at the exit plane. The horizontal and vertical axes correspond to the transverse dimensions of the domain scaled to the wavelength. The plotting limits are a subset of the full transverse domain in order to visually observe the speckle structure. Here, the mean intensity of the beam is $I_0 = 3.24 \times 10^{15}$ W/cm^2 which corresponds to $Q = 2.7$. The top panel clearly shows the initial speckle pattern with bright speckles appearing at intensities over five times the mean. These speckles will filament most strongly, breaking into smaller structures. This is apparent in the middle panel which illustrates the resulting speckle pattern after interaction with the plasma. The corresponding case with polarization smoothing is shown in Fig. 4 with the top and bottom panels showing the respective speckle pattern at the entrance and exit planes as before. The reduction in filamentation due to polarization smoothing is apparent if one compares Fig. 3(b) to Fig. 4(b). In making quantitative assessments, filamentation is most easily observed in k-space as a spreading of the initial Fourier distribution. Observations in physical

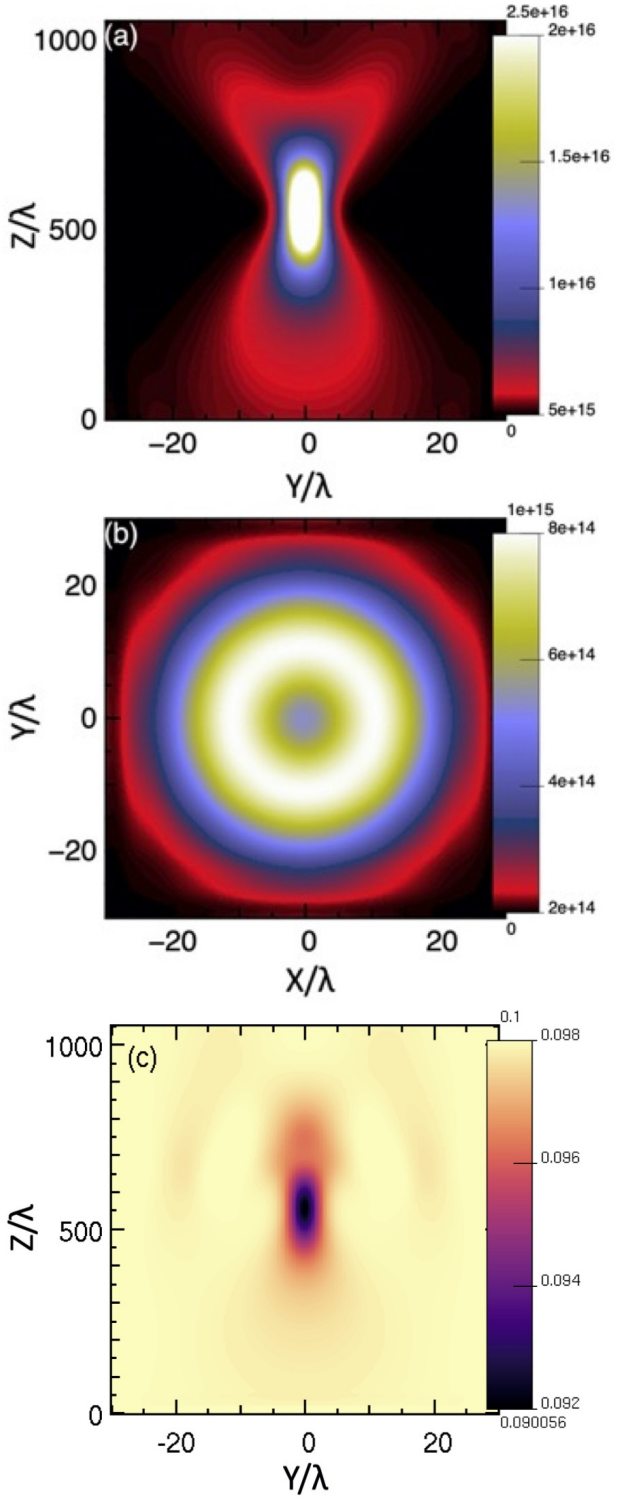

FIG. 1. The self-focusing of a single 3D Gaussian speckle at roughly twice the threshold power (a) in the y-z plane at $x = 0$, (b) in the x-y plane at $z = 945 \times \lambda_0$, and (c) the associated electron density in units of the critical density in the y-z plane at $x = 0$.

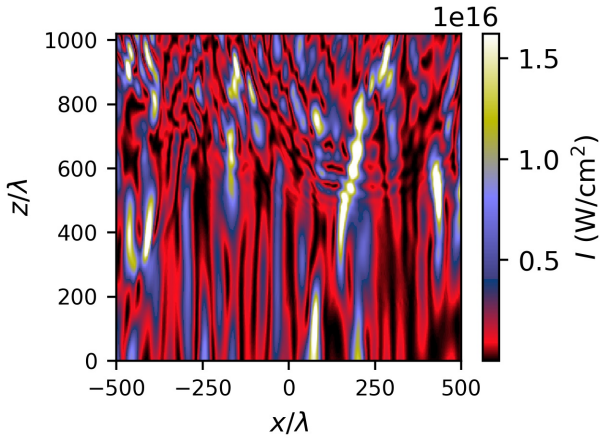

FIG. 2. Speckle pattern of an RPP beam plotted in the xz plane with z the direction of laser propagation. A smaller subset of the domain is selected for clarity of presentation. The mean intensity is 3.24×10^{15} W/cm^2 with a range of intensities following the RPP probability distribution function described in Eq. (9). The plasma consists of hydrogen with $n_e/n_c = 0.1$, $T_e = 3$ keV and $T_i = 1.5$ keV. Self-focusing is apparent over the first speckle length (512 λ) with breakup into smaller speckles apparent over the second speckle length.

space are complicated by the speckled pattern and the difficulty that arises in uniquely determining a speckle. In Fourier space, filamentation is quite obvious by the spreading of the power spectrum. This is most clearly seen in Fig. 5, which corresponds to the Fourier spectrum associated with the speckle pattern shown in Fig. 3(b). The initial Fourier representation of the beam is a disk of constant amplitude with radius $1/(2f)$ as shown by the dashed, white circle in the figure. The expansion of the power to large k vectors is indicative of filamentation. This spreading motivates the metrics that are defined in the next section.

III. METRICS

Four metrics are used to identify ponderomotive filamentation and determine the threshold Q. Of these, one is related to the intensity profile of the beam, one to the depth of the density perturbations associated with the intensely focused speckles, and two to the angular distribution and transverse size of the speckles.

The first metric is the fraction of power above $5I_0$, where I_0 is the average intensity of the beam. This metric is derived from the FOPAI, denoted as $F(I)$. For an RPP beam, the FOPAI is initially[29]

$$F_{RPP}(I) = \left(1 + \frac{I}{I_0}\right) e^{-I/I_0}, \tag{9}$$

where I is the intensity. For an RPP beam with PS, the

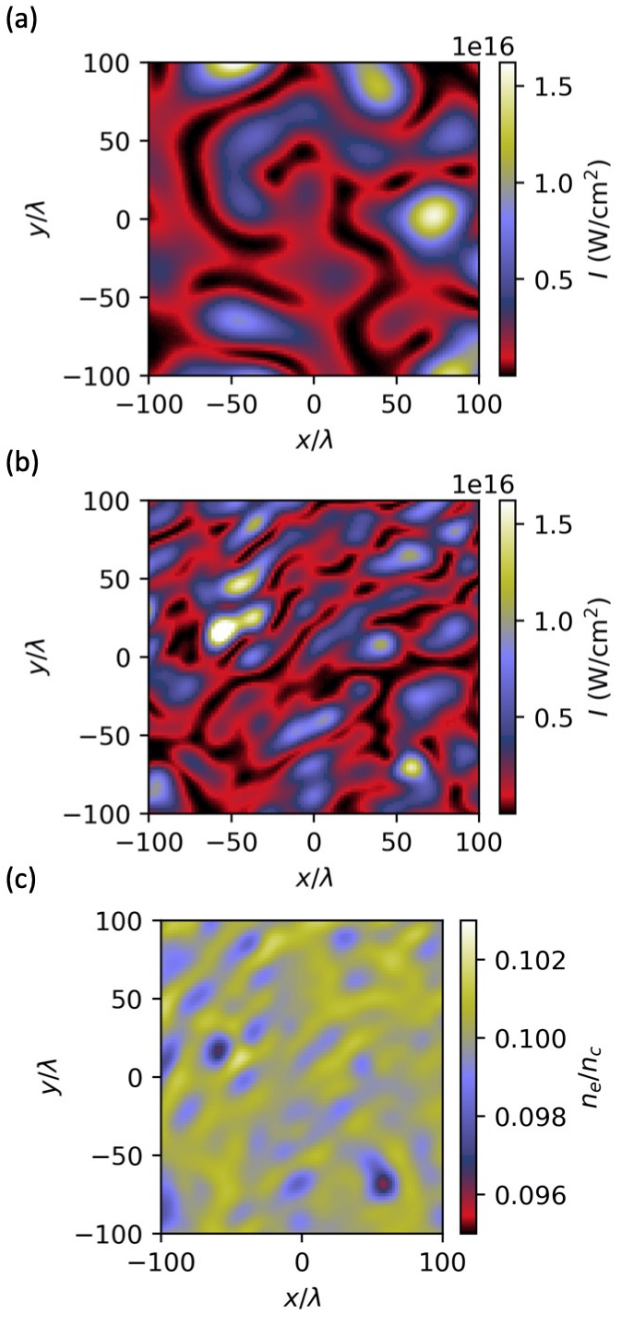

FIG. 3. Speckle pattern of an RPP beam (a) at the entrance plane and (b) after traveling through the domain (1024 wavelengths long) with the same average laser intensity and plasma parameters shown in Fig. 2. The breakup of the speckles into smaller speckles is apparent by comparing the top and middle panels. The bottom panel (c) shows the electron density associated with the beam at the same location as the middle panel. The deepest holes are correlated with the most intense speckles.

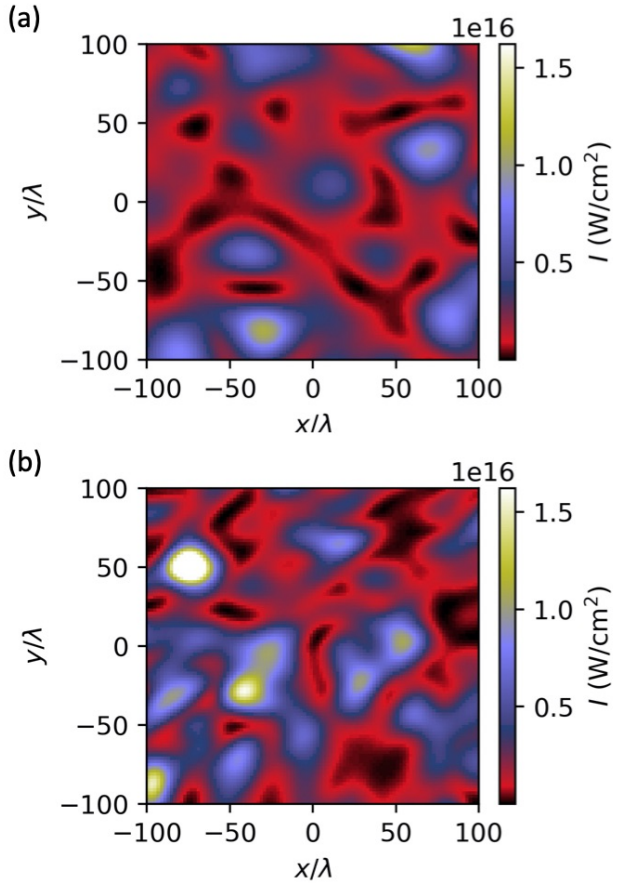

FIG. 4. Speckle pattern of an RPP beam with polarization smoothing (a) at the entrance plane and (b) after traveling through the domain (1024 wavelengths long) with the same average laser intensity and plasma parameters shown in Fig. 2. The breakup of the speckles into smaller speckles is apparent in comparing the top and bottom panels. Contrasting the bottom panel with Fig. 3(b), the reduction in filamentation due to the use of polarization smoothing is apparent.

FOPAI is initially[23]

$$F_{PS}(I) = \left(1 + \frac{2I}{I_0} + \frac{2I^2}{I_0^2}\right) e^{-2I/I_0}. \tag{10}$$

The above equations reflect the fact that polarization smoothing decreases the fraction of power at larger intensities thereby reducing the filamentation risk. Because there is no light absorption, the transversely averaged intensity is constant even in the presence of filamentation. The FOPAI can be computed numerically by performing a cumulative sum of an intensity weighted histogram of the spatially varying intensity. To assess filamentation, the maximum value of $F(5I_0)$ and its value at the exit plane of the simulation is determined. The FOPAI is evaluated at $5I_0$ so that it is sampling the tail of the intensity distribution where filamentation most strongly alters the intensity profile. An RPP beam traveling through a vacuum using the setup as defined in the previous section

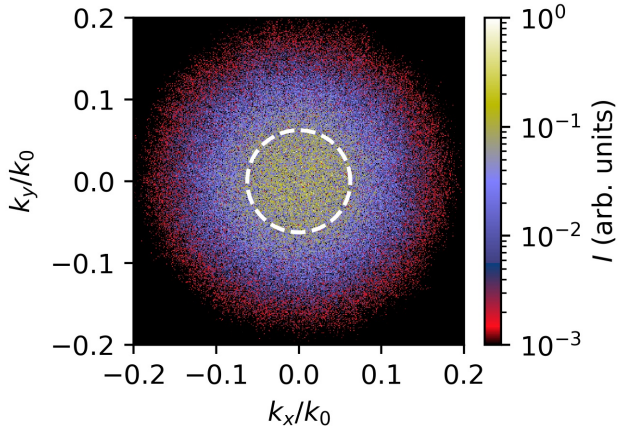

FIG. 5. The Fourier-space intensity distribution for a filamenting beam corresponding to the speckle pattern in Fig. 3(b). The initial intensity distribution is a constant value out to radius $1/(2f)$ as shown by the dashed, white circle. The spreading of the beam to larger perpendicular k vectors outside this circle is apparent. This is an indication of self-focusing and filamentation.

will conserve the value of $F(5I_0) = F_{RPP}(5I_0) \approx 0.04$ for an RPP beam and $F(5I_0) = F_{PS}(5I_0) \approx 0.0028$ with PS. When plasma causes the speckles to self-focus, $F(I)$ develops a larger tail in the distribution, and this is reflected in a larger value of $F(5I_0)$. This can be seen in Fig. 6(a), where the FOPAI for an RPP beam with $I_0 = 3.24 \times 10^{15}$ W/cm^2 in the presence of a plasma is plotted. If the RPP beam was propagating through vacuum, $F(I)$ would remain unchanged over the course of the simulation. Here, the curves are plotted at different axial locations with the blue, orange, green, and red curves corresponding to 0, 1, 2, and 4 speckle lengths, respectively. The blue curve is well described by Eq. (9). The FOPAI develops a large tail after one speckle length that subsequently relaxes as speckles filament into two or more smaller speckles with less power that are consequently less prone to further self-focusing. After four speckle lengths, the intensity distribution is nearly the same as the incident distribution, albeit with a larger number of speckles with less power in each.

The next metric characterizes the depth of the density holes produced near the region where the largest $F(5I_0)$ occurs. In Fig. 6(b), the fraction of rarefied density with deviation from the initial density exceeding $x = |\delta n/n|$ is shown. The initial and final distribution of density perturbations is nearly identical but the final power per speckle is below the threshold for further filamentation. The largest fraction of deep holes coincides with the location of largest FOPAI. Very large depressions occur for which linearized hydrodynamics is inadequate even if forced to be non-negative consistent with what is seen in Fig. 1(c).

For the next two metrics, an intensity weighted averag-

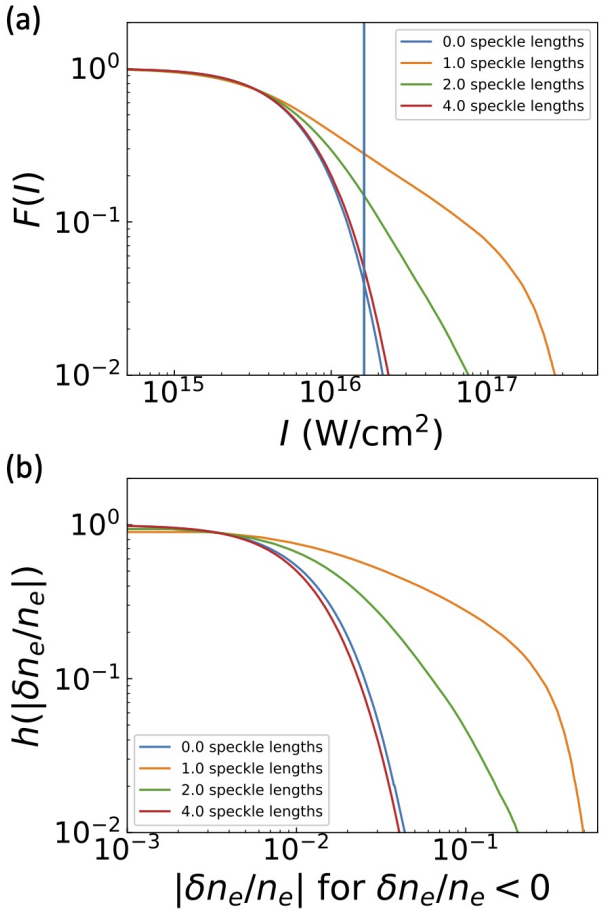

FIG. 6. (a)The FOPAI distribution for an RPP beam traveling through plasma with $I_0 = 3.24\times10^{15}$ W/cm^2. The plasma conditions are $n_e = 0.1n_c$, $T_e = 3$ keV, and $T_i = 1.5$ keV. The different lines correspond to increasing axial distance along the direction of propagation as shown in the legend. One speckle length is roughly 180 μm. The blue vertical line is the $5I_0$ line; it intersects the FOPAI line at the value of $F(5I_0)$. (b) The fraction of the initial density, n_l displaced by speckles that has an amplitude of perturbation exceeding $|\delta n/n_l| = x$

ing over the transverse wave numbers is performed. This is defined for a generic quantity, ψ as,

$$\langle\psi\rangle = \frac{\int \psi I(k) d^2k}{\int I(k) d^2k}. \tag{11}$$

Using this averaging procedure, the mean-square transverse wave number, κ^2, can be defined. This measures the angular dispersion of the beam. It is a composite metric, and is defined as

$$\kappa^2 = \frac{\langle k_\perp^2\rangle - k_{\perp 0}^2}{k_0^2} \tag{12}$$

where $k_{\perp 0}^2$ is the initial value of $\langle k_\perp^2\rangle$ which is unchanged in vacuum. Thus, κ^2 represents the change in $\langle k_\perp^2\rangle$ as the beam propagates through a plasma and self focuses,

developing larger perpendicular k-vectors, spreading in k space, and increasing κ^2. This can be seen when comparing the dashed, white circle in Fig. 5 with the resultant spread in the same figure. When the intensity is below the threshold for filamentation, little spreading beyond the dashed, white circle is seen. Above the filamentation threshold for a given speckle, the maximum unstable wavenumber, $k_\perp^{\max} = \sqrt{n_e/2n_c}(v_o/\bar{v}_e)(\omega/c)$. For the parameters considered here, $ck_\perp^{\max}/\omega$ is 0.074 for $I = I_0$ and 0.16 for $I = 5I_0$.

The third metric is f_{eff} or the effective f-number of the beam[44],

$$f_{\text{eff}} = \frac{1}{3\langle|k_\perp|\rangle}. \tag{13}$$

This metric allows for an effective f number to be computed as it changes due to interaction with the plasma. Prior to filamentation, $f_{\text{eff}} = f$. Because the f number is related to the speckle size, this metric can also be used to determine the variability of speckle size due to interaction with the plasma; the speckle width is $f\lambda_0$. When a beam begins to filament, self-focusing causes the speckle size to decrease. This is shown by comparing Fig. 3(a), the initial speckle pattern, with Fig. 3(b) where the speckles are visibly smaller after propagating through the plasma. This behavior of the beam is represented by the decrease in f_{eff}.

Relating f_{eff} and κ^2, $f_{\text{eff}} \sim 1/\sqrt{\langle k_\perp^2\rangle}$, so that as one decreases the other increases. However, due to the lower power of k in f_{eff}, it is not as sensitive to high $k_\perp$ modes as κ^2. Since $F(5I_0)$ is not explicitly dependent on the k-space distribution of intensities, it is the least sensitive to high $k_\perp$ modes. This means that significant numerical noise at high $k_\perp$ can complicate interpretation and comparison of these metrics. Further, the Feit and Fleck algorithm[47] is only valid for modes that satisfy the paraxial approximation. For this reason, a cutoff is introduced into Eqs. (12) and (13) at $k_\perp = k_0/\sqrt{2} \approx 0.7k_0$. To illustrate this, a characteristic intensity distribution is integrated along k_x and plotted against k_y in Fig. 7 for a filamenting (orange) and non-filamenting (blue) case. The broadening of the intensity profile as a function of k_y in the filamenting case reflects the spreading of the beam in the transverse directions.

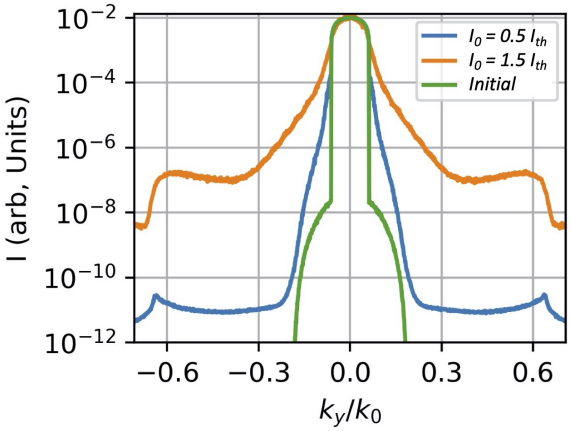

FIG. 7. The intensity distribution in k space summed along k_x and plotted against k_y. This is plotted for the initial distribution (green) and the distribution after passing through the plasma both for a filamenting (orange, $I_0 = 1.5I_{thr} = 1.8 \times 10^{15}$ W/cm^2) and non filamenting (blue, $I_0 = 0.5I_{thr} = 6.1 \times 10^{14}$ W/cm^2) case.

IV. RESULTS

To find the threshold Q, the simulations are performed as described in Sec. II with the average intensity varied. In this way, the threshold is determined by an intensity variation, though the plasma conditions could instead be varied. Two different beams are used for the study: an RPP beam without PS, and an RPP beam with PS. The intensities ranged from 0.4 to 3.25 $\times 10^{15}$ W/cm^2 for RPP only and from 0.76 to 5.2 $\times 10^{15}$ W/cm^2 for RPP+PS. The threshold is $I_{thr} = 1.22 \times 10^{15}$ W/cm^2. Here, I_{thr} corresponds to a value of $Q = 1$.

For each beam type and initial average intensity the steady state values of the four metrics are evaluated. The metrics, f_{eff} and κ^2 are evaluated at the last plane in the simulation so that they aggregate the entire interaction with the plasma with significant changes occurring while filamenting. These laser beam metrics are plotted versus initial average intensity in Fig. 8 with the top, middle, and bottom panel corresponding to $F(5I_0)$, f_{eff}, and κ^2, respectively. The orange and blue curves correspond to the associated metric with and without PS, respectively. From Fig. 8(a), it is difficult to discern a noticeable threshold from $F(5I_0)_{max}$ (the maximum value along the z direction); the slope of the metric changes gradually. For the lower intensities, the $F(5I_0)_{L_z}$ (the value after four speckle lengths) is the same as the maximum value. That is, the intensity increase does not lead to breakup (filamentation) of high intensity speckles but only to an increase caused the the refraction of the light into the density holes produced by the ponderomotive force. Only when that increase exceeds the filamentation threshold do the speckles breakup into smaller scales with less power per speckle. That is reflected by the decrease in $F(5I_0)$ at distances beyond the location of the maximum. As the intensity increases, the distance of the maximum of $F(5I_0)$ from the initial simulation boundary decreases. Examining the next panels (b) and (c) of Fig. 8, f_{eff} and κ^2 exhibit a dramatic change in f_{eff}, decreasing abruptly from its initial value of $f_{\text{eff}} = 8$, and similarly an abrupt increase in κ^2 above a certain threshold value. Further, the middle and bottom panels show that the RPP beam with PS has less severe filamentation even when the threshold is exceeded.

In order to extract a threshold for filamentation from the $F(5I_0)$ metric, the beam is defined to be filament-

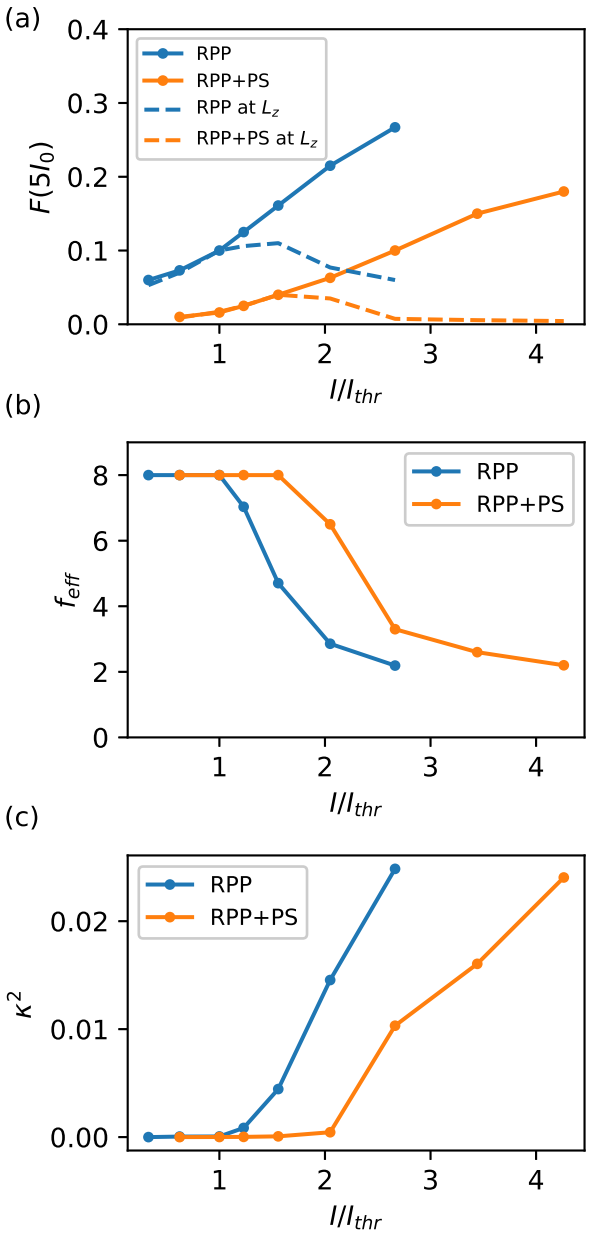

FIG. 8. Intensity scan of the three metrics with (a), (b), and (c) corresponding to $F(5I_0)$, $f_{\rm eff}$, and κ^2 respectively. A value of $I/I_{\rm thr} = 1$ with $I_{thr} = 1.22 \times 10^{15}$ W/cm^2 corresponds to $Q = 1$. The orange and blue curves correspond to an RPP beam with and without PS, respectively. The solid and dash curves in (a) are the maximum and at the exit plane respectively. The filamentation threshold is coincident with the intensity for which the solid and dashed curves diverge.

ing if the maximum value of $F(5I_0)$ exceeds the value at the exit plane. To be meaningful, the length of simulation in the propagation direction of the beams must be long enough for the filamentation process to complete. For high intensity, two speckle lengths are sufficient. For intensities near threshold, four speckle lengths are sufficient for RPP beams without PS. With PS, six speckle

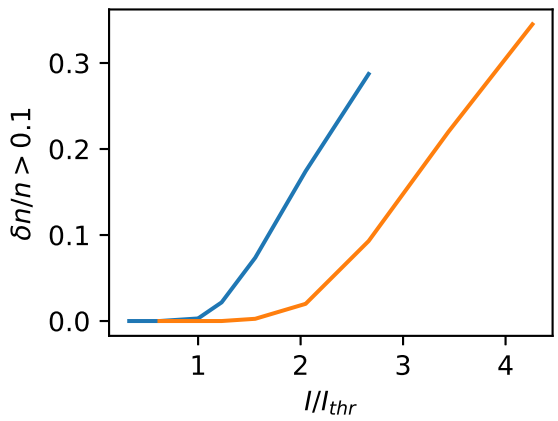

FIG. 9. The the fraction of the volume where the density depression is bigger than 0.1 is shown for an RPP beam (blue) and for an RPP+PS beam (orange). This metric increases abruptly above $I/I_{th} = 1$ for an RPP beam and above $I/I_{th} = 1.6$ for an RPP+PS beam.

lengths were needed. For the other two laser beam metrics, threshold is determined by $|f_{\rm eff} - f_{\rm vac}|/f_{\rm vac} > 1\%$ and $\kappa > 1\%$. Because we are plotting κ^2, this amounts to a threshold value of $\kappa^2 = 10^{-4}$. In these expressions, $f_{\rm vac} = 8$ corresponds to the initial f number as shown by the asymptotic value at low intensities in Fig. 8(a). To the precision of the intensity scan, all metrics result in a threshold value of $Q = 1.0$ for a simple RPP beam, and $Q = 1.6$ for an RPP beam with PS.

Finally, Fig. 9 shows the increase of large density depressions that occur once the filamentation thresholds are exceeded. This is the same metric as reported in Fig. 6(b). Here, the fraction of the volume where $\delta n/n$ is plotted versus I/I_{thr}. At intensities below the threshold for filamentation, this metric is relatively flat and near zero, indicating that linearized hydrodynamics is appropriate. Above threshold, however, the rapid increase indicates the necessity of a nonlinear hydrodynamic treatment.

V. CONCLUSION

In this paper, we examined the ponderomotive filamentation figure of merit for two different beam types: an RPP beam with and without polarization smoothing. The simulations neglect inverse-bremsstrahlung absorption in order to isolate this effect from, e.g., thermal filamentation. It is found that temporal convergence required reflecting boundary conditions in the axial direction for the fluid equations to avoid plasma escaping the domain. Periodic boundary conditions in the transverse directions are also employed. Damping and thermal conduction are included as important physical processes. Damping also aids in the development of a steady

state. After performing a spatial convergence study in the transverse direction (see Appendix A), it was found that $\Delta x = \Delta y = 0.5\lambda_0$ is sufficient. Higher resolution is needed as the threshold for ponderomotive filamentation is exceeded, especially for the metrics that depend on the tail of the distribution of intensity in k-space.

Once a steady state is reached, the metrics for filamentation are evaluated. The first metric, $F(5I_0)$, or fraction of power above $5I_0$, measures the intensity profile of the beam. The next metric measures the fraction of area of the plasma where the density depressions, $|\delta n/n| > 0.1$. Without self-focusing, this is a extremely small fraction of the plasma area in the focal plane. Above threshold, there is a dramatic increase. The other two metrics κ^2 and f_{eff} are nearly inverses of each other, and measure the angular dispersion of the beam and the effective f-number, respectively. The κ^2 metric could be used to develop a reduced model of filamentation to be employed in a ray-tracing description of the laser because it can be related to spreading of the beam through its interaction with the plasma. Defining the angle, θ, relative to the direction of incidence, $\tan\theta \approx \theta = k_\perp/k_0$, where the small angle approximation is consistent with the paraxial approximation underlying the description of the laser. With this relation, it is apparent that,

$$\left\langle \Delta\theta^2 \right\rangle = \kappa^2, \tag{14}$$

where $\left\langle \Delta\theta^2 \right\rangle$ can be thought of as the mean-square deflection angle of the laser as it interacts with the plasma. Given that the simulation has a defined length of plasma and that the deflection should scale linearly with this distance, the quantity, $\left\langle \Delta\theta^2 \right\rangle$ can be used to construct the quantity, $d\left\langle \theta^2 \right\rangle/ds$, through the relation,

$$\frac{d\left\langle \theta^2 \right\rangle}{ds} = \frac{\kappa^2}{L}, \tag{15}$$

where L is the length over which the beam is filamenting. Within a radiation-hydrodynamics code, the plasma conditions and intensity within a local volume could be used to generate an effective Q value through Eq. (1), and the corresponding value of κ^2 could then be determined via a table that captures the results of the simulations presented here. The ray could then be deflected accordingly using a statistical description of the scattering.

Using the converged simulations, an intensity scan is performed, and the corresponding metrics are determined. Threshold behavior is clearly exhibited by the $F(5I_0)$, f_{eff}, and κ^2 metrics in Fig. 8. The threshold is determined using the $F(5I_0)$ metric by determining the maximum value over the axial distance and subtracting the final value at the exit plane of the simulation. For f_{eff} and κ, threshold is determined by when the difference between f_{eff} and its initial value exceeds 1% and when κ exceeds 1%. The fraction of the volume with $\delta n/n > 0.1$ is also computed. At intensities below threshold, this fraction is negligible indicating the appropriateness of a linearized hydrodynamic treatment. Above threshold, this fraction grows, illustrating the need for a nonlinear hydrodynamic treatment. The thresholds determined in this way are consistent with each other for all metrics within the precision of the intensity scan. The determined threshold values for an RPP beam without and with PS are $Q = 1.0$ and $Q = 1.6$ respectively which agrees with that stated in previous work[26,29]. In these previous studies, plasmas with higher values of $\bar{Z}$ were used: Ref. 29 used a CH plasma, and Ref. 26 a CO_2 plasma. For that reason, the ion pressure term in Eq. (1) was previously neglected. Here, a hydrogen plasma is used, and it is found that for such a low $\bar{Z}$ medium, the ion pressure term must be included in Eq. (1).

Here, we have sought to provide a more rigorous examination of the ponderomotive filamentation threshold (filamentation figure of merit), Q, for spatially smoothed laser beams than is present in the existing literature. Pitfalls associated with performing these simulations have been identified with an emphasis on numerical convergence. The time to achieve steady state (longer than 100 ps in the cases considered here) can potentially exceed the time over which plasma conditions change or laser properties evolve in realistic experiments as they do when temporal beam smoothing is used. However, we have provided a fairly simple yet descriptive way to define such a threshold. This methodology could be extended to account for other smoothing techniques in the future.

Appendix A: Convergence

In this section, convergence is only examined in the transverse direction due to the sensitivity of filamentation to adequate resolution in that plane. Resolution in the longitudinal direction is adequate.

In order to obtain useful information, the metrics must approach a single value as a function of time (steady state), and this value must be adequately resolved so that finer transverse resolution would not greatly change the metric. Both numerical and physical damping of IAWs will cause this steady state to be achieved more rapidly. The chosen value of the damping coefficient requires between 100 and 200 ps to reach a steady state. This can be seen in Fig. 10 where all the metrics eventually approach a steady value in time regardless of the intensity of the beam. Above threshold, the $F(5I_0)$ metric converges most rapidly of the three laser beam metrics because the location where its maximum occurs must be less than the total length. In fact, the more intense beams converge fastest because their maximum occurs at distances less than a speckle length. The other two metrics are slow to converge because the plasma density fluctuations in the second, third, and higher ranks of speckles depend on the previous rank of speckles to settle down. This fact is the basis of the concept of plasma self-smoothing[45]

Next, spatial convergence in the transverse direction is assessed. Using all the settings listed in Sec. II, but vary-

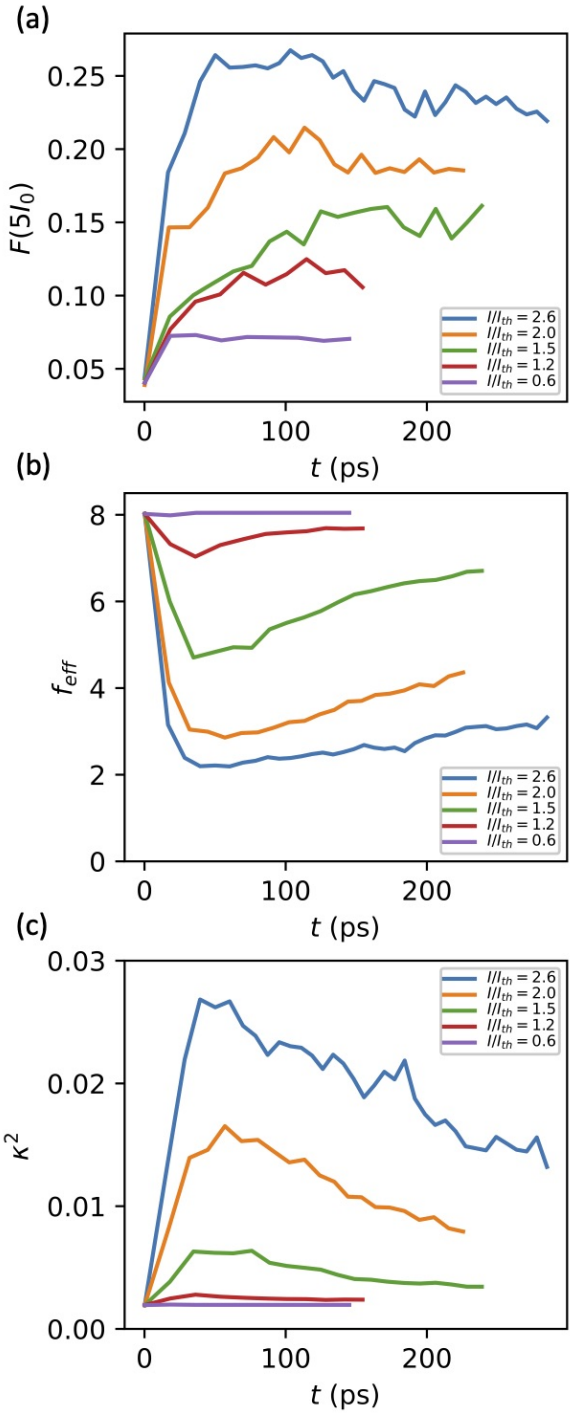

FIG. 10. The time evolution of all three metrics with (a), (b), and (c) corresponding to $F(5I_0)$, κ^2, and f_{eff}, respectively. The color of each curve corresponds to a different intensity ranging from 0.6 to 2.6 times $I_{thr} = 1.22 \times 10^{15}$ W/cm^2 as indicated by the legends.

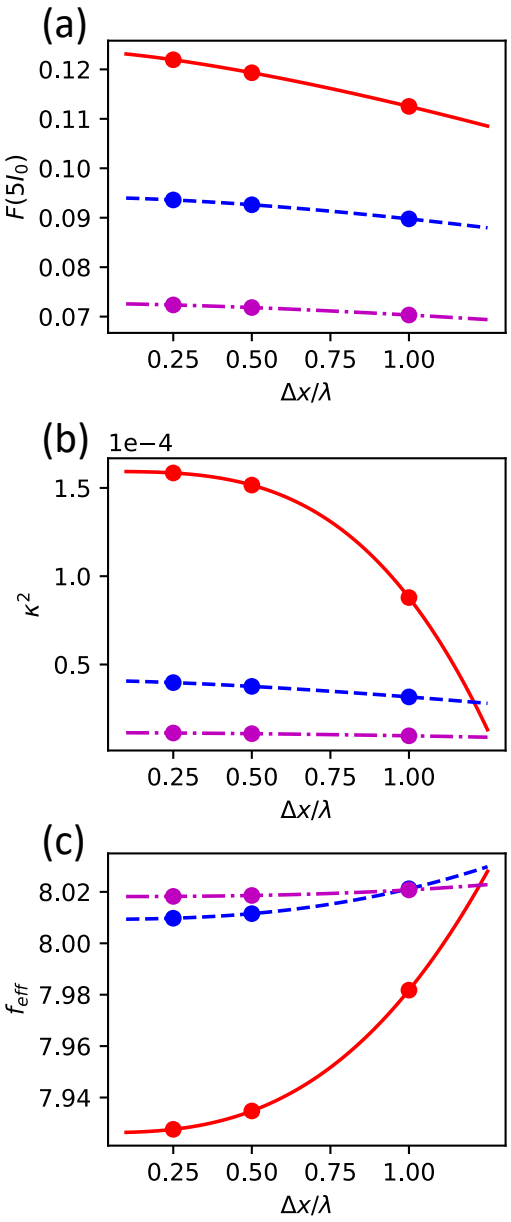

FIG. 11. (a) $F(5I_0)$, (b) κ^2, (c) and f_{eff} plotted versus resolution in the transverse direction. The magenta dash-dotted curve, cyan dashed curve, and red solid curve correspond to intensities of 6×10^{14}, 10^{15}, and 1.4×10^{15} W/cm^2. The points correspond to the metric at that intensity and resolution, and the curves are polynomial fits. Higher resolution is required for the κ^2 and f_{eff} metrics than for $F(5I_0)$ at higher intensities.

ing the transverse resolution by factors of two between λ_0 and $0.25\lambda_0$ it is found that $0.5\lambda_0$ is adequate to resolve the metrics. This is shown in Fig. 11 where all three metrics are plotted versus resolution for three different intensities. The top panel plots $F(5I_0)$, the middle panel κ^2, and the bottom panel f_{eff}. The magenta dash-dotted curve, cyan dashed curve, and red solid curve correspond to intensities of 6×10^{14}, 10^{15}, and 1.4×10^{15} W/cm^2. The lower intensity is below the self-focusing threshold, and little variation is seen in the metrics with resolution. As the intensity increases and self-focusing becomes pro-

nounced, more resolution is required especially for the metrics which depend strongly on the tail of the intensity distribution in k-space, κ^2 and f_{eff}. It is likely that if intensity is increased arbitrarily, greater resolution than chosen here would be needed to resolve self-focusing and filamentation. However, since it is the aim of this work to characterize the threshold at which self-focusing occurs, a resolution of $0.5\lambda_0$ is adequate. For arbitrarily large intensities, κ^2 and f_{eff} will not be reliable.

ACKNOWLEDGMENTS

The authors greatly appreciate helpful discussions with S. Brunner and W. Rozmus. This work was performed under the auspices of the U.S. Department of Energy by Lawrence Livermore National Laboratory under Contract DE-AC52-07NA27344. This document was prepared as an account of work sponsored by an agency of the United States government. Neither the United States government nor Lawrence Livermore National Security, LLC, nor any of their employees makes any warranty, expressed or implied, or assumes any legal liability or responsibility for the accuracy, completeness, or usefulness of any information, apparatus, product, or process disclosed, or represents that its use would not infringe privately owned rights. Reference herein to any specific commercial product, process, or service by trade name, trademark, manufacturer, or otherwise does not necessarily constitute or imply its endorsement, recommendation, or favoring by the United States government or Lawrence Livermore National Security, LLC. The views and opinions of authors expressed herein do not necessarily state or reflect those of the United States government or Lawrence Livermore National Security, LLC, and shall not be used for advertising or product endorsement purposes.

DATA AVAILABILITY

The data that support the findings of this study are available from the corresponding author upon reasonable request.

[1] N. L. Kugland, D. D. Ryutov, P.-Y. Chang, R. P. Drake, G. Fiksel, D. H. Froula, S. H. Glenzer, G. Gregori, M. Grosskopf, M. Koenig, Y. Kuramitsu, C. Kuranz, M. C. Levy, E. Liang, J. Meinecke, F. Miniati, T. Morita, A. Pelka, C. Plechaty, R. Presura, A. Ravasio, B. A. Remington, B. Reville, J. S. Ross, Y. Sakawa, A. Spitkovsky, H. Takabe, and H.-S. Park, Nat. Phys. **8**, 809 (2012).

[2] C. M. Huntington, F. Fiuza, J. S. Ross, A. B. Zylstra, R. P. Drake, D. H. Froula, G. Gregori, N. L. Kugland, C. C. Kuranz, M. C. Levy, C. K. Li, J. Meinecke, T. Morita, R. Petrasso, C. Plechaty, B. A. Remington, D. D. Ryutov, Y. Sakawa, A. Spitkovsky, H. Takabe, and H. S. Park, Nat. Phys. **11**, 173 (2015).

[3] O. A. Hurricane, D. A. Callahan, D. T. Casey, E. L. Dewald, T. R. Dittrich, T. Döppner, S. Haan, D. E. Hinkel, L. F. Berzak Hopkins, O. Jones, A. L. Kritcher, S. Le Pape, T. Ma, A. G. MacPhee, J. L. Milovich, J. Moody, A. Pak, H. S. Park, P. K. Patel, J. E. Ralph, H. F. Robey, J. S. Ross, J. D. Salmonson, B. K. Spears, P. T. Springer, R. Tommasini, F. Albert, L. R. Benedetti, R. Bionta, E. Bond, D. K. Bradley, J. Caggiano, P. M. Celliers, C. Cerjan, J. A. Church, R. Dylla-Spears, D. Edgell, M. J. Edwards, D. Fittinghoff, M. A. Barrios Garcia, A. Hamza, R. Hatarik, H. Herrmann, M. Hohenberger, D. Hoover, J. L. Kline, G. Kyrala, B. Kozioziemski, G. Grim, J. E. Field, J. Frenje, N. Izumi, M. Gatu Johnson, S. F. Khan, J. Knauer, T. Kohut, O. Landen, F. Merrill, P. Michel, A. Moore, S. R. Nagel, A. Nikroo, T. Parham, R. R. Rygg, D. Sayre, M. Schneider, D. Shaughnessy, D. Strozzi, R. P. J. Town, D. Turnbull, P. Volegov, A. Wan, K. Widmann, C. Wilde, and C. Yeamans, Nat. Phys. **12**, 800 (2016).

[4] C. C. Kuranz, H. S. Park, C. M. Huntington, A. R. Miles, B. A. Remington, T. Plewa, M. R. Trantham, H. F. Robey, D. Shvarts, A. Shimony, K. Raman, S. MacLaren, W. C. Wan, F. W. Doss, J. Kline, K. A. Flippo, G. Malamud, T. A. Handy, S. Prisbrey, C. M. Krauland, S. R. Klein, E. C. Harding, R. Wallace, M. J. Grosskopf, D. C. Marion, D. Kalantar, E. Giraldez, and R. P. Drake, Nat. Commun. **9**, 1564 (2018).

[5] P. Tzeferacos, A. Rigby, A. F. A. Bott, A. R. Bell, R. Bingham, A. Casner, F. Cattaneo, E. M. Churazov, J. Emig, F. Fiuza, C. B. Forest, J. Foster, C. Graziani, J. Katz, M. Koenig, C. K. Li, J. Meinecke, R. Petrasso, H. S. Park, B. A. Remington, J. S. Ross, D. Ryu, D. Ryutov, T. G. White, B. Reville, F. Miniati, A. A. Schekochihin, D. Q. Lamb, D. H. Froula, and G. Gregori, Nat. Commun. **9**, 591 (2018).

[6] A. L. Kritcher, D. C. Swift, T. Döppner, B. Bachmann, L. X. Benedict, G. W. Collins, J. L. DuBois, F. Elsner, G. Fontaine, J. A. Gaffney, S. Hamel, A. Lazicki, W. R. Johnson, N. Kostinski, D. Kraus, M. J. MacDonald, B. Maddox, M. E. Martin, P. Neumayer, A. Nikroo, J. Nilsen, B. A. Remington, D. Saumon, P. A. Sterne, W. Sweet, A. A. Correa, H. D. Whitley, R. W. Falcone, and S. H. Glenzer, Nature **584**, 51 (2020).

[7] J. F. Drake, P. K. Kaw, Y. C. Lee, G. Schmid, C. S. Liu, and M. N. Rosenbluth, The Physics of Fluids **17**, 778 (1974), https://aip.scitation.org/doi/pdf/10.1063/1.1694789.

[8] D. W. Forslund, J. M. Kindel, and E. L. Lindman, The Physics of Fluids **18**, 1002 (1975), https://aip.scitation.org/doi/pdf/10.1063/1.861248.

[9] W. Kruer, *The physics of laser plasma interactions* (Addison-Wesley Publishing Co. Inc, 1988).

[10] R. L. Berger, C. H. Still, E. A. Williams, and A. B. Langdon, Physics of Plasmas **5**, 4337 (1998), https://doi.org/10.1063/1.873171.

[11] P. Kaw, G. Schmidt, and T. Wilcox, Phys. Fluids **16**, 1522 (1973).

[12] B. I. Cohen, B. F. Lasinski, A. B. Langdon, and J. C. Cummings, Phys. Fluids B **3**, 766 (1991).

[13] R. L. Berger, B. F. Lasinski, T. B. Kaiser, E. A. Williams, A. B. Langdon, and B. I. Cohen, Physics of Fluids B: Plasma Physics **5**, 2243 (1993), https://doi.org/10.1063/1.860758.

[14] J. D. Lindl, P. Amendt, R. L. Berger, S. G. Glendinning, S. H. Glenzer, S. W. Haan, R. L. Kauffman, O. L. Landen, and L. J. Suter, Phys. Plasmas **11**, 339 (2004).

[15] D. E. Hinkel, M. B. Schneider, B. K. Young, A. B. Langdon, E. A. Williams, M. D. Rosen, and L. J. Suter, Phys. Rev. Lett , 195001 (2006).

[16] H. A. Rose and D. F. DuBois, Phys. Fluids B **5**, 590 (1993).

[17] J. Garnier, Phys. Plasmas **6**, 1601 (1999).

[18] P. J. Wegner, J. M. Auerbach, T. A. B. Jr., S. N. Dixit, J. K. Lawson, J. A. Menapace, T. G. Parham, D. W. Swift, P. K. Whitman, and W. H. Williams, in *Optical Engineering at the Lawrence Livermore National Laboratory II: The National Ignition Facility*, Vol. 5341, edited by M. A. Lane and C. R. Wuest, International Society for Optics and Photonics (SPIE, 2004) pp. 180 – 189.

[19] E. I. Moses, R. N. Boyd, B. A. Remington, C. J. Keane, and R. Al-Ayat, Phys. Plasmas **16**, 041006 (2009).

[20]T. Boehly, D. Brown, R. Craxton, R. Keck, J. Knauer, J. Kelly, T. Kessler, S. Kumpan, S. Loucks, S. Letzring, *et al.*, Optics Commun. **133**, 495 (1997).
[21]J.-L. MIQUEL, D. BATANI, and N. BLANCHOT, Review of Laser Engineering **42**, 131 (2020).
[22]J. W. Goodman, *Statistical Optics* (Wiley, 1985).
[23]E. Lefebvre, R. L. Berger, A. B. Langdon, B. J. MacGowan, J. E. Rothenberg, and E. A. Williams, Physics of Plasmas **5**, 2701 (1998), https://doi.org/10.1063/1.872957.
[24]S.N. Dixit, D. Munro, J.R. Murray, M. Nostrand, P.J. Wegner, D. Froula, C.A. Haynam, and B.J. MacGowan, J. Phys. IV France **133**, 717 (2006).
[25]S. Skupsky, R. W. Short, T. Kessler, R. S. Craxton, S. Letzring, and J. M. Soures, J. Appl. Phys. **66**, 3456 (1989).
[26]E. L. Dewald, S. H. Glenzer, O. L. Landen, L. J. Suter, O. S. Jones, J. Schein, D. Froula, L. Divol, K. Campbell, M. S. Schneider, J. Holder, J. W. McDonald, C. Niemann, A. J. Mackinnon, and B. A. Hammel, Plasma Physics and Controlled Fusion **47**, B405 (2005).
[27]C. H. Still, R. L. Berger, A. B. Langdon, D. E. Hinkel, L. J. Suter, and E. A. Williams, Physics of Plasmas **7**, 2023 (2000), https://doi.org/10.1063/1.874055.
[28]C. E. Max, Phys. Fluids **19**, 74 (1976).
[29]E. A. Williams, Physics of Plasmas **13**, 056310 (2006), https://doi.org/10.1063/1.2179051.
[30]K. Estabrook, W. L. Kruer, and D. S. Bailey, The Physics of Fluids **28**, 19 (1985), https://aip.scitation.org/doi/pdf/10.1063/1.865180.
[31]A. J. Schmitt, The Physics of fluids **31**, 3079 (1988).
[32]A. J. Schmitt, Physics of Fluids B: Plasma Physics **3**, 186 (1991), https://doi.org/10.1063/1.859936.
[33]E. M. Epperlein, Phys. Rev. Lett. **65**, 2145 (1990).
[34]V. Y. Bychenkov, W. Rozmus, and V. Tikhonchuk, Phys. Rev. Lett. **75**, 4405 (1995).
[35]A. V. Brantov, V. Y. Bychenkov, and V. Tikhonchuk, JETP **83**, 716 (1996).
[36]A. V. Brantov, V. Y. Bychenkov, W. Rozmus, and C. E. Capjack, Phys. Rev. Lett. **93**, 125002 (2004).
[37]A. V. Brantov, V. Y. Bychenkov, and W. Rozmus, Phys. Rev. Lett. **108**, 205001 (2012).
[38]V. Y. Bychenkov, W. Rozmus, A. V. Brantov, and V. Tikhonchuk, Phys. Plasmas **7**, 1511 (2000).
[39]R. L. Berger, E. Valeo, and S. Brunner, Physics of Plasmas **12**, 062508 (2005), https://doi.org/10.1063/1.1931089.
[40]S. Weber, G. Riazuelo, P. Michel, R. Loubére, F. Walraet, V. T. Tikhonchuk, V. Malka, J. Ovadia, and G. Bonnaud, Laser Part. Beams **22**, 189 (2004).
[41]W. B. Mori, C. Joshi, J. M. Dawson, D. W. Forslund, and J. M. Kindel, Phys. Rev. Lett. **60**, 1298 (1988).
[42]E. Higson, R. Trines, J. Jiang, R. Bingham, K. L. Lancaster, J. R. Davies, and P. A. Norreys, New Journal of Physics **15**, 015027 (2013).
[43]C. Ruyer, A. Debayle, P. Loiseau, P. E. Masson-Laborde, J. Fuchs, M. Casanova, J. R. Marquès, L. Romagnani, P. Antici, N. Bourgeois, M. Nakatsutsumi, M. Safronova, M. Starodubtsev, and T. Lin, Physics of Plasmas **28**, 052701 (2021), https://doi.org/10.1063/5.0043931.
[44]A. V. Maximov, I. G. I. G. Ourdev, D. Pesme, W. Rozmus, V. T. Tikhonchuk, and C. E. Capjack, Physics of Plasmas **8**, 1319 (2001), https://doi.org/10.1063/1.1352056.
[45]A. J. Schmitt and B. B. Afeyan, Phys. Plasmas **5**, 503 (1998), https://doi.org/10.1063/1.872733.
[46]T. W. Johnston and J. M. Dawson, Physics of Fluids **16**, 722 (1973).
[47]M. D. Feit and J. A. Fleck, J. Opt. Soc. Am. B **5**, 633 (1988).
[48]J. A. F. Hittenger, "Mfh multifluid hydro package for pf3d," Tech. Rep. (LLNL, 2005).
[49]A. Bell, Phys. Fluids **28**, 2007 (1985).